Chapter 2

Methodology for Reactive Power Management in Grid-Tied PV System with Coordinated Control Strategy

2.1 Introduction

The grid-tied solar photovoltaic (PV) inverter is generally used to provide active power (P) support to the distribution grid operated at maximum power point (MPP) condition. However, the PV systems not only provide active power supply but also inject reactive power into the distribution grid without extra cost and mechanism. According to the IEEE Standard 1547, the grid-tied PV inverters are allowed to actively participate in grid voltage support by providing reactive power into the distribution grid. Therefore, to properly manage the flow of real and reactive power into the grid, an appropriate control scheme is mandatory in grid-tied PV system. Moreover, an appropriate range of reactive power (Q) should be known at MPP condition to ensure satisfactory operation of the grid-tied PV system. This chapter presents an improved mathematical methodology to derive the P-Q capability curve of grid-tied PV system for managing the reactive power injection into the grid at MPP conditions for various environmental conditions. The proposed methodology is used to obtain reactive power limits of a single-stage three-phase PV system connected to a distribution grid by evaluating all the possible sets of working points within the stable region of operation. The improved methodology provides the basis for selecting the reference to the controllers and accordingly manages the active and reactive power injection into the grid. An experimental prototype is developed, and the test results are carried out using a real-time simulator OPAL-RT OP-4510 to evaluate the effectiveness of the proposed methodology. Experimental and simulation results verify the reactive power limits of PV system implemented with PI-based DC-link voltage and current controller in coordination with maximum power point tracking (MPPT) controller. To validate the effectiveness of the proposed mathematical methodology, the environmental conditions are varied and the corresponding reactive power injections to the grid under MPP condition are measured. These measured values are compared with the P-Q values obtained from the mathematical methodology presented in this work.

2.2 System Architecture and Control Strategy of the Grid-Tied PV System

The system configuration of the grid-tied PV system is presented in Fig. 2.1. The solar photovoltaic (PV) array is connected to the grid through a voltage source inverter (VSI) and a low-pass LCL filter at the point of interconnection. As shown in Fig. 2.1., the inductor and resistor of the inverter side filter is denoted as L_{if} and R_{if}; the capacitor and resistor of the filter is denoted as C_{f} and R_{c}; the inductor and resistor of the grid side filter is denoted as L_{of} and R_{of}; the equivalent inductor and resistor of the grid is indicated as L_{g} and R_{g}, and m_{a}, m_{b} and m_{c} denotes the modulation signals which are used for the gate pulse generation using sinewave pulse width modulation (SPWM). The output current and voltage from the PV array is indicated as i_{PV} and v_{PV}; v_{dc} is the voltage across the DC-link capacitor c_{dc}; the grid voltage and grid current are represented as v_{gabc} and i_{gabc}; P_{g} and Q_{g} is the active power and reactive power delivered to the grid. The grid-tied PV system has only a single stage that utilizes the VSI to extract maximum power from the PV array and transfer it to the grid. is designed for proper injection of active as well as reactive power into the grid.

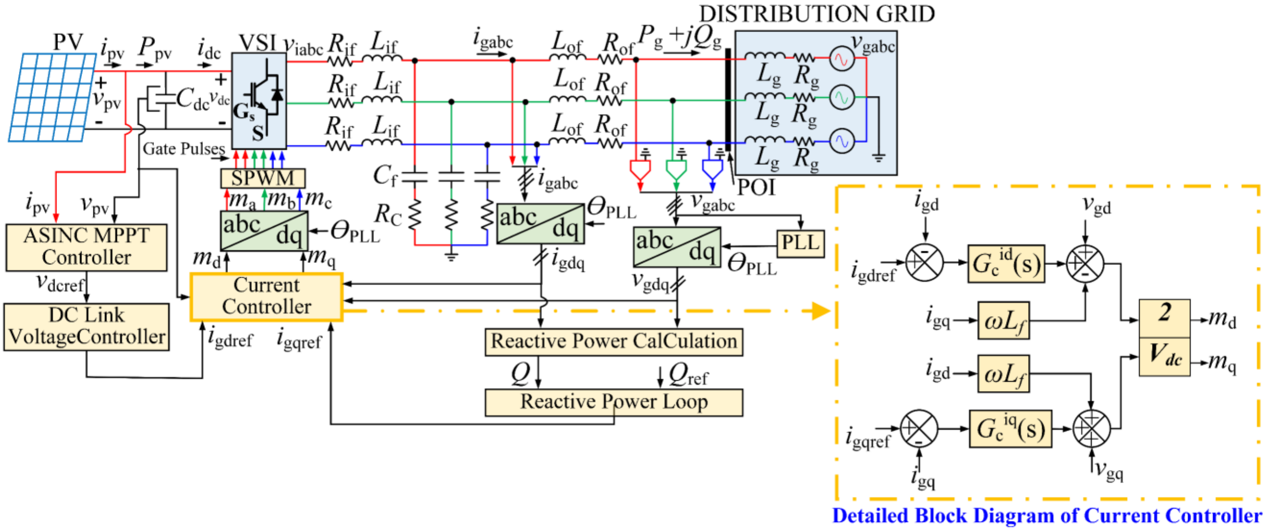

Fig. 2.1. System configuration of the grid-tied PV system.

The grid-tied PV system control architecture, as shown in Fig. 2.1, has four significant fragments: 1) grid synchronization phase-locked loop (PLL), 2) DC-link voltage controller, 3) adaptive step size INC MPPT controller, and 4) current controller. The control strategy applied to the grid-tied PV system mainly consists of two cascaded loops, the fast internal current control loop, which regulates the grid current, and an external voltage control loop, which controls the DC-link voltage. The DC-link voltage controller is used to control the PV array DC output voltage according to the reference given by the MPPT controller. The grid injected current is controlled according to the PV array real power output and the required reactive power. The complete control strategy is implemented in a synchronous reference frame (*dq* reference frame) also called as *dq* control. The synchronous reference frame phase-locked loop (SRF-PLL) as discussed in [103] is used in this work to achieve grid synchronization. The SRF-PLL processes the voltage signals and generates phase angle and grid frequency. The phase angle is used to transform the grid voltages and currents in *abc* natural reference frame to synchronously rotating *dq* frame. Further, the transformed current variables are processed in the current controller and are transformed back from the *dq* frame into the *abc* reference frame. The output of the current controller is the modulating signals for the grid-tied VSI. These modulating signals are compared with a high-frequency carrier wave in the sinusoidal pulse width modulation (SPWM) scheme and generate the gating pulse for the grid-tied VSI. The detailed discussion of the PLL, MPPT controller, DC-ink voltage controller, and the current controller is explained in the following subsections.

2.2.1 Phase-Locked Loop

The grid voltage's phase angle and amplitude are the basic information for the grid-tied PV system. The SRF-PLL is the most popular and widely employed scheme for extracting grid voltage phase, frequency, and amplitude for grid-synchronization of the VSI of the PV system [103]. The phase angle (θ) is estimated from the grid voltage's angular frequency (ω). However, the magnitude information is obtained in the process of extracting phase information. The three-phase balanced grid voltage can be mathematically expressed as

$$\begin{bmatrix} v_{\mathrm{ga}} \\ v_{\mathrm{gb}} \\ v_{\mathrm{gc}} \end{bmatrix} = \begin{bmatrix} V_{\mathrm{m}} \cos(\omega_{\mathrm{g}} t) \\ V_{\mathrm{m}} \cos(\omega_{\mathrm{g}} t - 120) \\ V_{\mathrm{m}} \cos(\omega_{\mathrm{g}} t + 120) \end{bmatrix} \tag{2.1}$$

where $\theta_{\mathrm{g}} = \omega_{\mathrm{g}}\mathrm{t}$. Applying Clarke's transformation to (2.1)

$$\begin{bmatrix} v_{\mathrm{g}\alpha} \\ v_{\mathrm{g}\beta} \end{bmatrix} = \frac{2}{3} \begin{bmatrix} 1 & -\frac{1}{2} & -\frac{1}{2} \\ 0 & \frac{\sqrt{3}}{2} & -\frac{\sqrt{3}}{2} \end{bmatrix} \begin{bmatrix} v_{\mathrm{ga}} \\ v_{\mathrm{gb}} \\ v_{\mathrm{gc}} \end{bmatrix} = \mathrm{V_m} \begin{bmatrix} \cos\theta_{\mathrm{g}} \\ -\sin\theta_{\mathrm{g}} \end{bmatrix} \tag{2.2}$$

Applying the Park's transformation to (2.2)

$$\begin{bmatrix} v_{\mathrm{gd}} \\ v_{\mathrm{gq}} \end{bmatrix} = \begin{bmatrix} \cos\theta & -\sin\theta \\ \sin\theta & \cos\theta \end{bmatrix} \begin{bmatrix} v_{\mathrm{g}\alpha} \\ v_{\mathrm{g}\beta} \end{bmatrix} = \begin{bmatrix} \mathrm{V_m} \cos(\theta_{\mathrm{g}} - \theta) \\ \mathrm{V_m} \sin(\theta_{\mathrm{g}} - \theta) \end{bmatrix} \tag{2.3}$$

In (2.3), if it is controlled to reach θ_g which is $\theta_g = \theta$, the synchronization is achieved. That means the inverter output signals have the same frequency and phase as the grid. Then, (2.3) can be expressed as

$$\begin{bmatrix} v_{gd} \\ v_{gq} \end{bmatrix} = \begin{bmatrix} V_m \\ 0 \end{bmatrix} \tag{2.4}$$

If it is assumed that θ_g-θ is very small then from (2.3) $v_{gq} = V_m(\theta_g-\theta)$.

The angular frequency (ω) of the PLL can be represented as

$$\omega = \frac{d\theta}{dt} = G_c^{PLL}.v_q \tag{2.5}$$

where G_c^{PLL} is the transfer function of the PI controller.

The SRF-PLL regulates the q component of the transformed signals to zero, and thus the PI controller attains the phase angle and frequency. The phase angle provided by this PLL estimates the phase angle of the positive sequence component of the balanced set of input signal that coincides with the phase angle of the phase a signal. Hence, the PLL frequency ω and the phase angle θ can track the grid frequency ω_g and phase angle θ_g, respectively, by the proper design of the controller Gc^{PLL}. By taking Laplace transform of (2.5),

$$s\theta(s) = V_m(s)(\theta_g(s) - \theta(s))G_c^{PLL}(s) \tag{2.6}$$

The expression given in (2.6) can be represented in the control system block diagram as the linearized model of PLL as depicted in Fig. 2.2. It is observed from Fig.2.2 that with a feedback control loop, v_q is regulated to zero and the phase angle of the grid voltages can be captured as θ. The control structure block diagram of the SRF-PLL is illustrated in Fig. 2.3. From Figs.2.2 and 2.3, the plant transfer function of the SRF-PLL is expressed as

$$G_p(s) = \frac{V_m}{s} \tag{2.7}$$

By using (2.7), the PI controller G_c^{PLL} (s) is designed to achieve zero steady-state error in v_q.

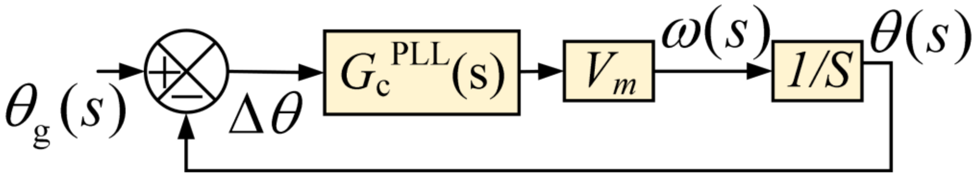

Fig. 2.2. Linearized Model of the SRF-PLL.

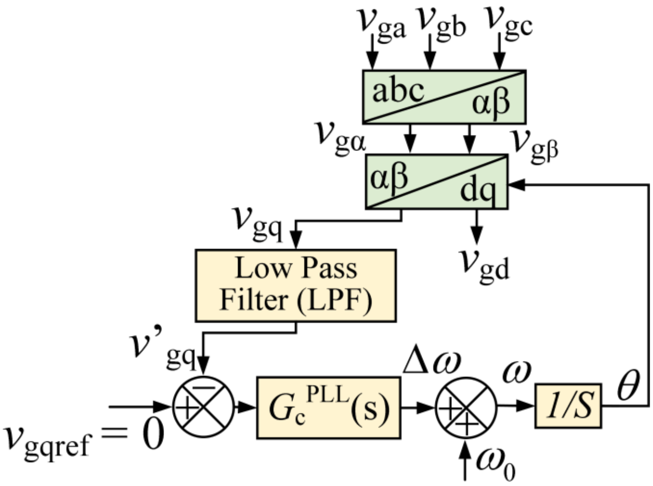

Fig. 2.3. Control Structure of the SRF-PLL.

2.2.2 Maximum Power Point Tracking Controller

The MPPT controller aims to track the MPP irrespective of variations in atmospheric conditions to confirm that maximum available power is extracted from the PV panel. The MPP tracking technique continuously regulates the PV voltage to extract maximum power with changes in irradiance and temperature. The two most popular and commonly used MPPT methods are incremental conductance (INC) and perturb and observe method (PO) [104]. The PO method is the simplest to implement. However, the PO method does not perform properly under rapidly varying environmental conditions [105]. Hence, the INC algorithm provides a solution to this problem. The INC is based on the slope of the power characteristics of the PV array. The maximum power is obtained when this slope is zero, which is expressed as

$$\frac{dp_{pv}}{dv_{pv}} = \frac{d(i_{pv} * v_{pv})}{dv_{pv}} = i_{pv} + v_{pv}\frac{di_{pv}}{dv_{pv}} = 0\,. \tag{2.8}$$

From the expression given in (2.8) condition for the INC can be expressed as

$$\left.\begin{array}{lll} \dfrac{di_{pv}}{dv_{pv}} + \dfrac{i_{pv}}{v_{pv}} = 0; & \dfrac{dp_{pv}}{dv_{pv}} = 0, & \text{at MPP} \\[2ex] \dfrac{di_{pv}}{dv_{pv}} + \dfrac{i_{pv}}{v_{pv}} > 0; & \dfrac{dp_{pv}}{dv_{pv}} > 0, & \text{at the right of MPP} \\[2ex] \dfrac{di_{pv}}{dv_{pv}} + \dfrac{i_{pv}}{v_{pv}} < 0; & \dfrac{dp_{pv}}{dv_{pv}} < 0, & \text{at the left of MPP} \end{array}\right\} \tag{2.9}$$

The accuracy and tracking speed of the INC algorithm depends on the fixed voltage step size. It is decided by considering the trade-off between steady-state oscillations and tracking time. An adaptive step size INC (ASINC) MPPT has been adapted to track the MPP to overcome this design dilemma [106]. A variable voltage step size based on the slope is used, which is higher at a large slope (far away from MPP) and decreases near the MPP. Thus, tracking time is reduced with almost negligible oscillations at MPP. The flowchart of the ASINC MPPT controller is illustrated in Fig. 2.4. The variable step size S_{step}, which depends on the slope of the PV characteristics can be expressed as

$$V_{\text{st}} = n\left|\frac{v_{\text{pv}}(k)i_{\text{pv}}(k) - v_{\text{pv}}(k-1)i_{\text{pv}}(k-1)}{v_{\text{pv}}(k) - v_{\text{pv}}(k-1)}\right| \tag{2.10}$$

where i_{pv}(k), v_{pv}(k) and n are the PV array current, PV array voltage at kth sampling instant and the scaling coefficient.

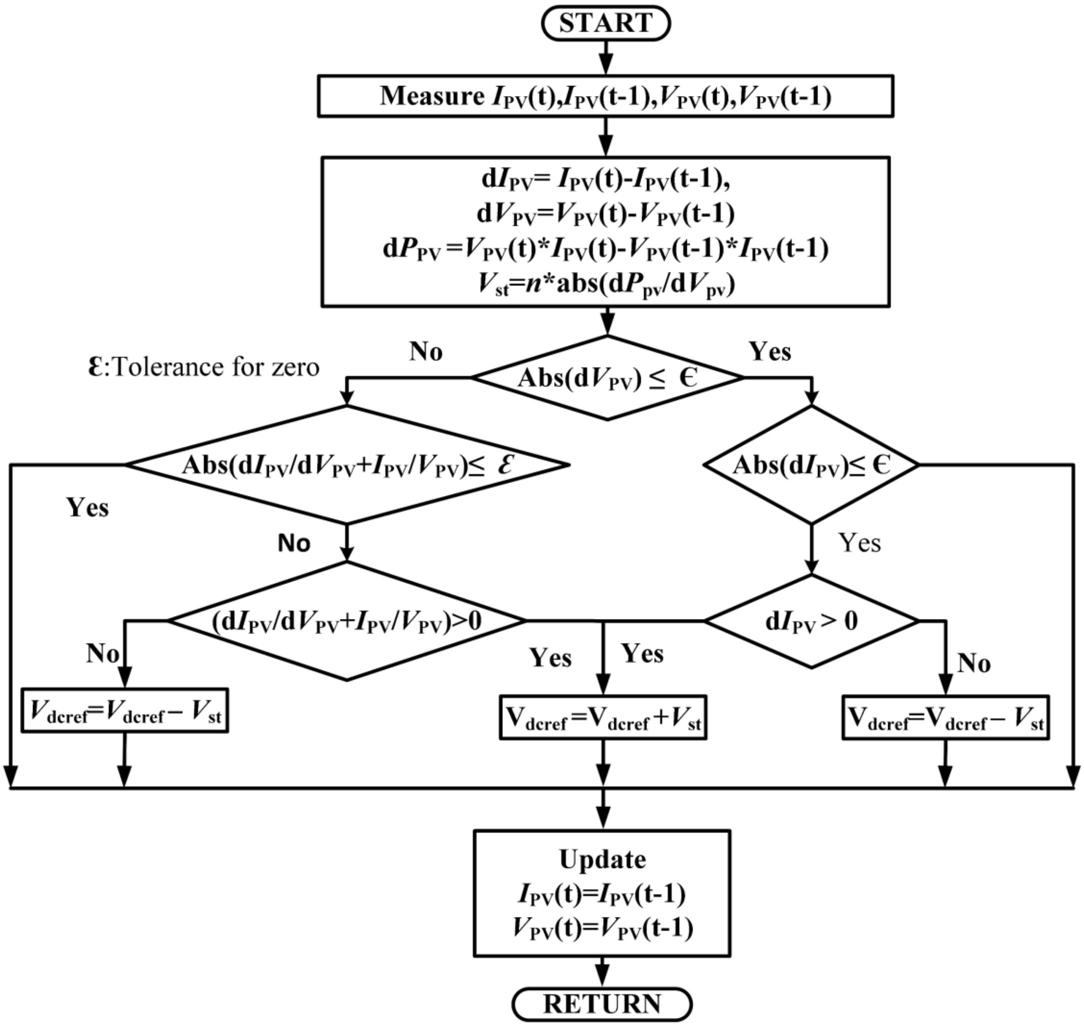

Fig. 2.4. Flow chart of the ASINC MPPT controller.

2.2.3 DC link Voltage Controller Design

The DC-link voltage controller is adopted to control the PV DC-link capacitor voltage v_{dc} as per reference v_{dcref} specified by the MPPT controller [107]. As the inverter is coupled to the grid, its output voltage is constant. Hence the current injected into the grid varies depending upon the power output of the PV array. The DC-link voltage controller controls the *d*-axis grid current, which regulates the real power injected into the grid. If the input DC power is larger than the power injected to the grid, the DC capacitor's voltage increases. Similarly, if the output grid power is larger than the input DC power, the voltage across the capacitor decreases. The DC-link voltage controller is based on the feedback linearization (FBL) technique as shown in Fig. 2.5 [108]. The mathematical model describing DC-link capacitor voltage dynamics based on the flow of real power is given by,

$$P_{\mathrm{grid}} = P_{\mathrm{PV}} - C_{\mathrm{dc}} v_{\mathrm{dc}} \frac{dv_{\mathrm{dc}}}{dt} \tag{2.11}$$

where $P_{\mathrm{grid}} = (3/2) v_{\mathrm{gd}} i_{\mathrm{gd}}$ and $P_{\mathrm{PV}} = \mathrm{v_{PV} i_{PV}}$. The given in (2.11) can be simplified as

$$C_{\mathrm{dc}} \frac{dv_{\mathrm{dc}}}{dt} = i_{\mathrm{PV}} - \frac{3 v_{\mathrm{gd}} i_{\mathrm{gd}}}{2 v_{\mathrm{dc}}} \tag{2.12}$$

where i_{gd} and v_{gd} are the *d*-axis grid current and grid voltage; v_{dc} and i_{PV} denote the DC-link voltage and the PV current, respectively.

It can be noted that (2.12) is not in the form of a linear time-invariant (LTI) system. The nonlinearity in (2.12) is introduced by i_{pv}, which is a nonlinear function of v_{PV}. This expression can be linearized using the FBL technique [109]. According to the FBL technique, (2.12) can be expressed in the following form

$$\dot{x} = f(x) + g(x) u_{\mathrm{i}} \tag{2.13}$$

Using the control input u_{i} as

$$u_{\mathrm{i}} = \frac{1}{g(x)} [u_{\mathrm{v}} - f(x)] \tag{2.14}$$

The nonlinearities can be canceled out as

$$\dot{x} = u_{\mathrm{v}} \tag{2.15}$$

Considering $\mathrm{i_{gd}}$ as a new control input, (2.14) can be expressed into a simple LTI system as follows

$$C_{\mathrm{dc}} \frac{dv_{\mathrm{dc}}}{dt} = u_{\mathrm{v}} \tag{2.16}$$

From (2.16), the plant transfer function is derived as

$$G_{\mathrm{p}}(s) = \frac{v_{\mathrm{dc}}(s)}{u_{\mathrm{v}}(s)} = \frac{1}{s C_{\mathrm{dc}}} \tag{2.17}$$

From the plant transfer function, a PI controller $G_c{}^{v_{dc}}$ for the DC-link voltage is formulated with appropriate settling time (ten times that of the current controller) and phase margin. The overall control scheme of the DC-link voltage controller is shown in Fig. 2.5, showing the conversion of intermediate signal u_V into i_d .

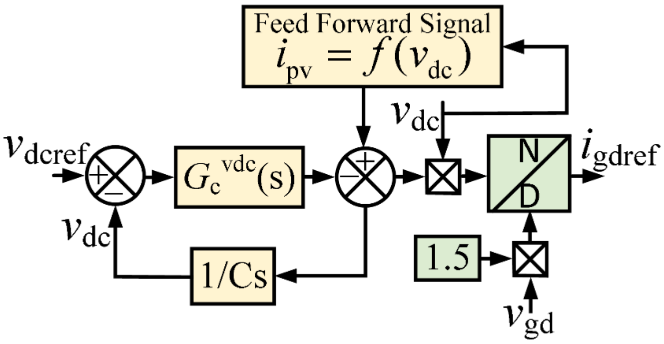

Fig. 2.5. Block diagram of the DC-link voltage controller.

2.2.4 Current Controller Design

The main objective of the current controller is to inject a sinusoidal current meeting the requirements of the grid on power quality and dynamic performance [110]. Also, the current controller regulates the active and reactive power injected to the grid [111]. The active power reference is responsible for the *d*-axis current reference, while the *q*-axis current reference generation is based on the reactive power requirement. The i_{dref} is obtained from the output of DC-link voltage controller and i_{qref} is obtained by using the formula Q_{ref} = (3/2) $*v_{gq}*i_{qref}$, where Q_{ref} is the required reactive power reference. The current controllers generate the sinusoidal modulating signals and control the output voltage v_i of the VSI, which in turn controls the grid current, and accordingly the active and reactive powers are controlled. The control structure block diagram of the current controller is demonstrated in Fig. 2.6.

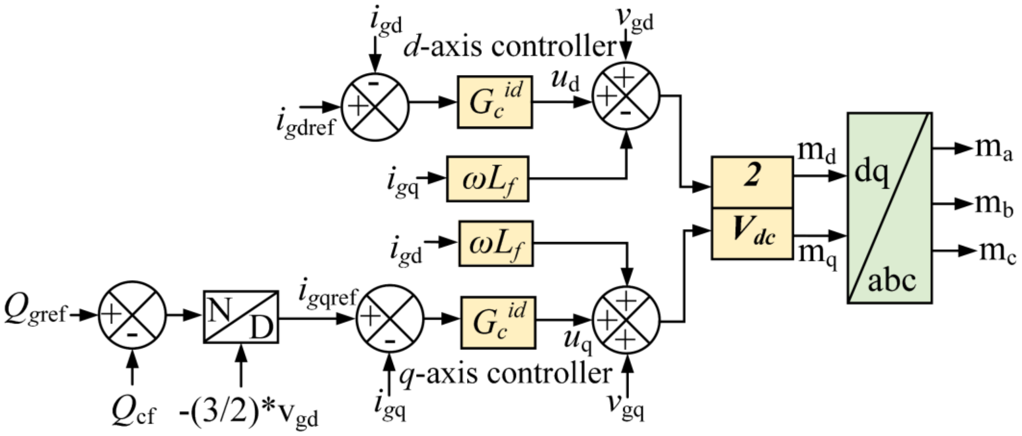

Fig. 2.6. Control structure block diagram of the current controller.

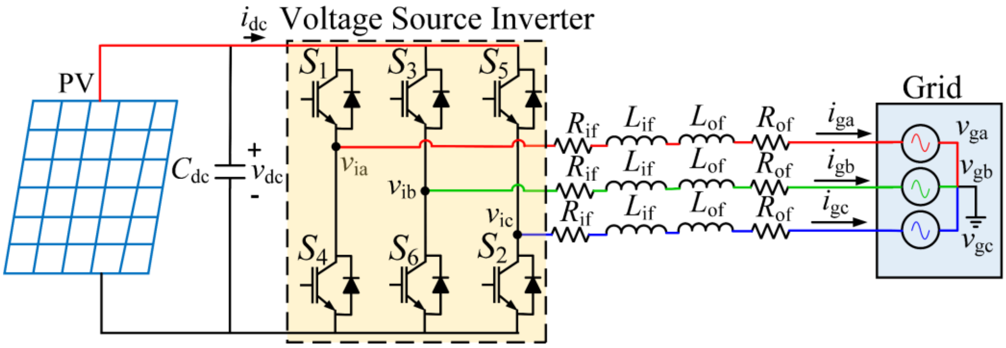

Fig. 2.7. Three-phase voltage source inverter connected with the grid.

The current controller is designed on the basis of the current dynamics of the filter. Fig. 2.7 shows a VSI, connected to the grid through an RL filter. The PV voltage is assumed as a constant DC voltage source for the analysis and design of the current controller. The dynamic equations consisting of the output voltages of the VSI, the grid voltages, and the output currents can be expressed as follows

$$\left.\begin{aligned} L_{\mathrm{f}}\frac{di_{\mathrm{ga}}}{dt} &= -R_{\mathrm{f}}i_{\mathrm{ga}} + v_{\mathrm{ia}} - v_{\mathrm{ga}} \\ L_{\mathrm{f}}\frac{di_{\mathrm{gb}}}{dt} &= -R_{\mathrm{f}}i_{\mathrm{gb}} + v_{\mathrm{ib}} - v_{\mathrm{gb}} \\ L_{\mathrm{f}}\frac{di_{\mathrm{gc}}}{dt} &= -R_{\mathrm{f}}i_{\mathrm{gc}} + v_{\mathrm{ic}} - v_{\mathrm{gc}} \end{aligned}\right\} \tag{2.18}$$

where i_{gabc}, v_{gabc} and v_{iabc} are the currents injected to the grid, the grid voltages and the output voltages of the VSI in the *abc* reference frame, respectively. $L_{\mathrm{f}} = L_{\mathrm{if}} + L_{\mathrm{of}}$ and $R_{\mathrm{f}} = R_{\mathrm{if}} + R_{\mathrm{of}}$ are the filter inductance and resistance, respectively.

The dynamic equations given in (2.18) can be transformed into the stationary reference frame by using Clark’s transformation as follows

$$L_{\mathrm{f}}\begin{bmatrix} \dfrac{di_{\mathrm{g}\alpha}}{dt} \\ \dfrac{di_{\mathrm{g}\beta}}{dt} \end{bmatrix} = -R_{\mathrm{f}}\begin{bmatrix} i_{\mathrm{g}\alpha} \\ i_{\mathrm{g}\beta} \end{bmatrix} + \begin{bmatrix} v_{\mathrm{i}\alpha} - v_{\mathrm{g}\alpha} \\ v_{\mathrm{i}\beta} - v_{\mathrm{g}\beta} \end{bmatrix} \tag{2.19}$$

where $i_{\mathrm{g}\alpha\beta}$, $v_{\mathrm{g}\alpha\beta}$ and $v_{\mathrm{i}\alpha\beta}$ indicate the grid currents, the grid voltages and the VSI output voltages in the $\alpha\beta$-reference frame.

By transforming (2.19) to *dq* reference frame and solving them

$$\begin{bmatrix} \dfrac{di_{\mathrm{g}d}}{dt} \\ \dfrac{di_{\mathrm{g}q}}{dt} \end{bmatrix} = \begin{bmatrix} \dfrac{-R_{\mathrm{f}}}{L_{\mathrm{f}}} & -\omega \\ \omega & \dfrac{-R_{\mathrm{f}}}{L_{\mathrm{f}}} \end{bmatrix}\begin{bmatrix} i_{\mathrm{g}d} \\ i_{\mathrm{g}q} \end{bmatrix} + \frac{1}{L_{\mathrm{f}}}\begin{bmatrix} v_{\mathrm{i}d} - v_{\mathrm{g}d} \\ v_{\mathrm{i}q} - v_{\mathrm{g}q} \end{bmatrix} \tag{2.20}$$

Splitting (2.20) into d-axis and q axis components,

$$\frac{di_{\mathrm{gd}}}{dt}=\frac{-R_{\mathrm{f}}}{L_{\mathrm{f}}}i_{\mathrm{gd}}-wi_{gq}+\frac{1}{L_{\mathrm{f}}}\left(v_{\mathrm{id}}-v_{\mathrm{gd}}\right) \tag{2.21}$$

$$\frac{di_{\mathrm{gq}}}{dt}=\frac{-R_{\mathrm{f}}}{L_{\mathrm{f}}}i_{\mathrm{gq}}+wi_{gd}+\frac{1}{L_{\mathrm{f}}}\left(v_{\mathrm{iq}}-v_{\mathrm{gq}}\right) \tag{2.22}$$

The expression given in (2.21), which is a *d*-axis equation, also contains a q-axis component. So, to cancel the coupling terms in (2.21), it is simplified and expressed in the following form

$$\frac{di_{\mathrm{gd}}}{dt}=\frac{-R_{\mathrm{f}}}{L_{\mathrm{f}}}i_{\mathrm{gd}}+\frac{1}{L_{\mathrm{f}}}\left(u_{\mathrm{gd}}\right) \tag{2.23}$$

where u_{gd} can be expressed as

$$u_{\mathrm{gd}}=v_{\mathrm{id}}-v_{\mathrm{gd}}-wL_{\mathrm{f}}i_{gq} \tag{2.24}$$

Therefore to generate the required u_{gd}, the inverter output voltage v_{id} should satisfy,

$$v_{\mathrm{id}}=u_{\mathrm{gd}}+v_{\mathrm{gd}}+wL_{\mathrm{f}}i_{gq} \tag{2.25}$$

Similarly, the simplified expression for the q-axis current from (2.22) can be derived as,

$$\frac{di_{\mathrm{gq}}}{dt}=\frac{-R_{\mathrm{f}}}{L_{\mathrm{f}}}i_{\mathrm{gq}}+\frac{1}{L_{\mathrm{f}}}\left(u_{\mathrm{gq}}\right) \tag{2.26}$$

where u_{gd} can be expressed as

$$u_{\mathrm{gq}}=v_{\mathrm{iq}}-v_{\mathrm{gq}}+wL_{\mathrm{f}}i_{gd} \tag{2.27}$$

The inverter output voltage is expressed as

$$v_{\mathrm{idq}}=m_{dq}\frac{v_{dc}}{2} \tag{2.28}$$

From (2.23) and (2.26), the plant transfer function can be expressed as

$$G_{\mathrm{pc}}(s)=\frac{i_{\mathrm{dq}}(s)}{u_{\mathrm{dq}}(s)}=\frac{1}{\left(R_f+sL_f\right)} \tag{2.29}$$

PI controllers for both *d* and *q* axes are designed based on the plant transfer function.

2.3 Approximate Model for the *P-Q* Capability Curve of the Grid-Tied PV System

The approximate simplified model of the grid-tied PV system is represented by a single line diagram as shown in Fig. 2.8. This model is derived without losing the accuracy to evaluate the *P-Q* capability curve of grid-tied PV system. The capability curve of the PV inverter determines the region of reactive power, where the PV inverter can continuously operate without crossing the physical limits of all the devices connected within the system.

The capability curve serves as an effective tool to quickly infer about the system operating point and the practicality of these curves have been verified for the system under study. The *P*-*Q* capability curve helps to determine the total apparent power generated by the grid-tied inverter. Also, reactive power-sharing can be gathered based on the *P*-*Q* capability curve of the inverter

2.4 Improved Methodology for the *P*-*Q* Capability Curve

The objective of the improved methodology is to determine the set of points (*P*, *Q*) to derive the *P*-*Q* capability curve at the MPP condition. The *P*-*Q* capability curve provides the limiting
value for the reactive power reference used for the current controller of the grid-tied PV system
operated at MPP for different environmental conditions. This methodology can improve the reactive power sharing of the grid-tied PV system. To evaluate the capability curve of the approximate model shown in Fig. 2.8, the following assumptions are taken

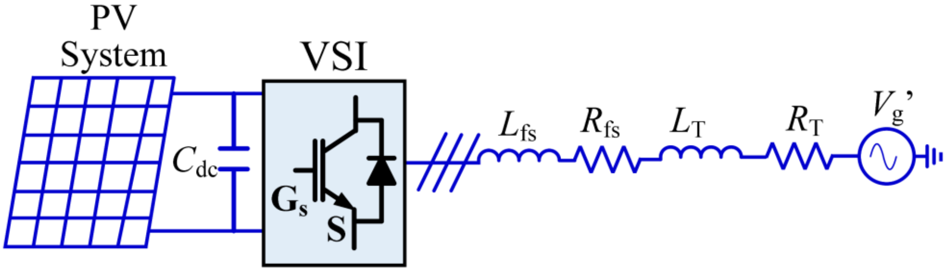

Fig. 2.8 Approximate simplified model of a grid -tied PV system.

- At the point of interconnection, the equivalent impedance of the approximate simplified network is represented as R_T in series with L_T, and v_g is the equivalent value of rated grid voltage. According to the park's transformation, v_g at the *d*-axis is formulated as

$$\begin{aligned} v_{gd}' &= v_g \\ v_{gq}' &= 0 \end{aligned} \tag{2.30}$$

- Neglecting the shunt branch of the passive filter, the reactive power fed by the filter's shunt branch is incorporated, while deciding the Q_{ref} of the current controller.

The relationship of *dq* components of inverter output voltages v_{id} and v_{iq} with the PV array is given as

$$\left.\begin{aligned} v_{id} &= \frac{v_{pv}}{2} m_a \cos\delta \\ v_{iq} &= -\frac{v_{pv}}{2} m_a \sin\delta \end{aligned}\right\} \tag{2.31}$$

where δ is the phase angle of the fundamental frequency component of the grid voltage v_g' and m_a is the modulation index of the VSI. By considering the above assumptions, the steady-state current flowing in the series branch of the filter can be obtained as

$$\left.\begin{aligned} i_{\mathrm{gd}} &= \frac{R(v_{\mathrm{id}} - v_{\mathrm{gd}}{}') - \omega L v_{\mathrm{iq}}}{\mathrm{R_e}^2 + (\omega L_e)^2} \\ i_{\mathrm{gq}} &= \frac{R v_{\mathrm{iq}} - \omega L(v_{\mathrm{id}} - v_{\mathrm{gd}}{}')}{\mathrm{R_e}^2 + (\omega L_e)^2} \end{aligned}\right\} \tag{2.32}$$

where $R_e = R_{\mathrm{Tg}} + R_\mathrm{f}$ and $L_e = L_{\mathrm{Tg}} + L_\mathrm{f}$. L_{Tg} and R_{Tg} represent the equivalent inductance and resistance at the PV side, and R_f and L_f represent the series filter resistance and inductance. The active power (P_g) and reactive power (Q_g) are given by

$$\left.\begin{aligned} P_g &= \frac{3}{2} v_{gd}{}' i_{gd} \\ Q_g &= \frac{3}{2} v_{gd}{}' i_{gq} \end{aligned}\right\} \tag{2.33}$$

From (2.32) and (2.33), the delivered P_g and Q_g from the solar PV is obtained as

$$\left.\begin{aligned} P_g &= \frac{3}{2} v_{gd}{}' * \frac{R(v_{\mathrm{id}} - v_{\mathrm{gd}}{}') - \omega L v_{\mathrm{iq}}}{\mathrm{R_e}^2 + (\omega L_e)^2} \\ Q_g &= \frac{3}{2} v_{gd}{}' * \frac{R v_{\mathrm{iq}} - \omega L(v_{\mathrm{id}} - v_{\mathrm{gd}}{}')}{\mathrm{R_e}^2 + (\omega L_e)^2} \end{aligned}\right\} \tag{2.34}$$

The capability curve has been obtained by evaluating (2.31) and (2.34) in the MATLAB environment for different values of m_a in the range of (0,1) and δ in the range of (0, $\pi/2$) for delivering positive active power.

The current and voltage relationship of the PV array is represented as

$$i_{\mathrm{pv}} = I_{sc}\left(1 - A e^{\left(\frac{v_{pv} - V_{oc}}{B}\right)}\right) \tag{2.35}$$

$$B = \frac{V_{MPP}}{I_{MPP}}\left(I_{sc} - I_{MPP}\right) \tag{2.36}$$

$$A = \frac{V_{MPP}}{I_{MPP}}\left(1 - \frac{I_{MPP}}{I_{sc}}\right) e^{-\left(\frac{V_{MPP} - V_{OC}}{B}\right)} \tag{2.37}$$

It has been observed from (2.31) and (2.34) that P_g and Q_g depend not only on m_a and δ but also on PV voltage. As PV voltage depends on m_a and δ, the PV voltage is obtained by using power balance relationship on both sides of the inverter. Neglecting the inverter losses, the power balance expression can be written as

$$v_{\mathrm{pv}}.i_{pv} = v_{\mathrm{id}}.i_{gd} + v_{\mathrm{gq}}.i_{gq} \tag{2.38}$$

By substituting (2.32) in (2.38),

$$v_{\mathrm{pv}}.i_{pv} = \frac{R_{\mathrm{e}} v_{\mathrm{id}}{}^2 - R_{\mathrm{e}} v_{\mathrm{gd}}{}' v_{\mathrm{id}} + R_{\mathrm{e}} v_{\mathrm{iq}}{}^2 - \omega L_{\mathrm{e}} v_{\mathrm{gd}}{}' v_{\mathrm{iq}}}{R_{\mathrm{e}}{}^2 + \left(\omega L_{\mathrm{e}}\right)^2} \tag{2.39}$$

From (2.31) and (2.39),

$$i_{pv} = \frac{3\left\{R_{\mathrm{e}}\left(\frac{m_a}{2}\right)^2 .v_{\mathrm{pv}} - \frac{m_a v_{\mathrm{gd}}{}'\left(\mathrm{R_e}\cos\delta - \omega L_e \sin\delta\right)}{2}\right\}}{2\left(R_{\mathrm{e}}{}^2 + \left(\omega L_{\mathrm{e}}\right)^2\right)} \tag{2.40}$$

From (2.35) and (2.40),

$$I_{sc}\left(1 - Ae^{\left(\frac{v_{pv}-V_{oc}}{B}\right)}\right) - \frac{3\left\{R_{\mathrm{e}}\left(\frac{m_a}{2}\right)^2 .v_{\mathrm{pv}} - \frac{m_a v_{\mathrm{gd}}{}'\left(\mathrm{R_e}\cos\delta - \omega L_e \sin\delta\right)}{2}\right\}}{2\left(R_{\mathrm{e}}{}^2 + \left(\omega L_{\mathrm{e}}\right)^2\right)} = 0 \tag{2.41}$$

Consider (2.41) as a function $f(v_{pv})$,

$$f(v_{pv}) = I_{sc}\left(1 - Ae^{\left(\frac{v_{pv}-V_{oc}}{B}\right)}\right) - \frac{3\left\{R_{\mathrm{e}}\left(\frac{m_a}{2}\right)^2 .v_{\mathrm{pv}} - \frac{m_a v_{\mathrm{gd}}{}'\left(\mathrm{R_e}\cos\delta - \omega L_e \sin\delta\right)}{2}\right\}}{2\left(R_{\mathrm{e}}{}^2 + \left(\omega L_{\mathrm{e}}\right)^2\right)} \tag{2.42}$$

From (2.42), the solution for PV voltage is obtained, when $f(\mathrm{v_{pv}})=0$

To solve this complex nonlinear equation, Newton-Raphson method [112] is considered. The first and second derivatives of (2.42) can be calculated as

$$\left.\begin{aligned} f'(v_{pv}) &= I_{sc}\frac{A}{B}e^{\left(\frac{v_{pv}-V_{oc}}{B}\right)} + \frac{3R_{\mathrm{e}}\left(\frac{m_a}{2}\right)^2 .v_{\mathrm{pv}}}{2\left(R_{\mathrm{e}}{}^2 + \left(\omega L_{\mathrm{e}}\right)^2\right)} \\ f''(v_{pv}) &= I_{sc}\frac{A}{B^2}e^{\left(\frac{v_{pv}-V_{oc}}{B}\right)} \end{aligned}\right\} \tag{2.43}$$

It is clear that the function $f(v_{PV})$ is increasing for $f'(v_{PV})> 0$ and convexing for $f''(v_{PV})>0$ for all values of v_{PV}. The Newton-Raphson method is converging for $f'(v_{PV}) > 0$.

Considering the initial value of PV voltage $v_{\mathrm{PV}} = V_{pvoc}$ the sequence of the process of the Newton-Raphson method is obtained as,

$$\left.\begin{aligned} v_{pv,o} &= V_{pvoc} \\ v_{pv,n+1} &= V_{pv,n} - \frac{f\left(v_{pv,n}\right)}{f^{'}\left(v_{pv,n}\right)} \end{aligned}\right\} \tag{2.44}$$

where *n* is the number of iterations. This sequence converges to the solution of v_{PV} within ten iterations. By varying m_a and δ, v_{PV} is calculated and various further points on *P* and *Q* curve are obtained.

The above methodology is improved to draw the *P-Q* capability curve at the MPP condition. It provides a unique cluster of m_{a} and δ pair points for a particular environmental condition. The formulation of the equation to obtain that cluster for drawing capability curve under MPP conditions for a specific irradiance and temperature are as follows:

Considering another function $f(m_{\mathrm{a}})$ with fixed PV voltage, V_{MPP} is defined by using both sides of (2.42)

$$f(m_a) = I_{sc}\left(1 - Ae^{\left(\frac{v_{pv}-V_{oc}}{B}\right)}\right) - \frac{3\left\{R_{\mathrm{e}}\left(\frac{m_a}{2}\right)^2 .V_{\mathrm{MPP}} - \frac{m_a v_{\mathrm{gd}}^{'}\left(\mathrm{R_e}\cos\delta - \omega L_e \sin\delta\right)}{2}\right\}}{2\left(R_{\mathrm{e}}^{2} + \left(\omega L_{\mathrm{e}}\right)^2\right)} \tag{2.45}$$

The above nonlinear equation is solved to obtain the values of m_{a} by using a numerical method considering a set of values of δ in increasing order with an increment of 0.005. The upper and lower limits of δ are not in the range $(0, \pi/2)$, as in the previous case. These limits are different for different environmental conditions for the stable region of the capability curve and determined by solving (2.45). The solution of the above equation is obtained when $f(\mathrm{m_a})=0$.

The expression given in (2.45) can be solved by using the Newton-Raphson method. The first derivative of (2.45) is obtained as

$$f^{'}(m_a) = \frac{3\left\{\frac{v_{\mathrm{gd}}^{'}\left(\mathrm{R_e}\cos\delta - \omega L_e \sin\delta\right)}{2}\right\}}{2\left(R_{\mathrm{e}}^{2} + \left(\omega L_{\mathrm{e}}\right)^2\right)} \tag{2.46}$$

It is clear that the function $f(m_{\mathrm{a}})$ increases as $f'(m_a) > 0$ for all values of m_{a}. The sequence of the process of Newton's method is expressed as

$$\left.\begin{aligned} m_a &= 1 \\ m_{a_{n+1}} &= m_{a_n} - \frac{f\left(m_n\right)}{f^{'}\left(m_n\right)} \end{aligned}\right\} \tag{2.47}$$

Using (2.47), the value of m_a can be obtained for a particular δ under MPP condition for a specific environmental condition, which is subsequently used to evaluate the reactive and real powers injected into the grid as a function of control parameters m_a and δ. Thus, a *P*-*Q* capability curve at the MPP condition is obtained. The effect of change in irradiance and temperature of the PV array can be expressed as

$$\left.\begin{aligned} I_{scn} &= I_{sc}\left(\frac{S}{1000}\right)+0.0014\left(T-25\right) \\ V_{ocn} &= V_{oc}-0.167\left(T-25\right)-2.3\left(1-\frac{S}{1000}\right) \\ V_{MPPn} &= V_{MPP}-0.167\left(T-25\right)-1.5\left(1-\frac{S}{1000}\right) \\ P_{MPPn} &= P_{MPP}\left(\frac{S}{1000}\right)\left(1-0.0052\left(T-25\right)\right) \end{aligned}\right\} \qquad (2.48)$$

Table 2.1 System and Control Parameters

	Description	Symbol	Simulation Value	Experimental Value
System Parameters	Grid Voltage Amplitude	V_g	415 V (L-L rms)	120 V (L-L rms)
	Grid frequency	f_g	50 Hz	50 Hz
	Switching frequency	f_{sw}	10 kHz	10 kHz
	Grid inductance	L_g	12 mH	1.5 mH
	Inverter side inductance	L_{if}	45 mH	6.2 mH
	Filter capacitance	C_f	186 µF	10 µF
	Grid side inductance	L_{of}	8 mH	1 mH
	DC link capacitance	C_{DC}	10000 µF	4700 µF
	PV open circuit voltage	V_{PVoc}	1085 V	540 V
	PV short circuit current	I_{PVsc}	480 A	9.6 A
	PV MPP voltage	V_{MPP}	850 V	430 V
	PV MPP current	I_{MPP}	442 V	8.72 A
	PV Maximum power	P_{MPP}	375 kW	3.75 kW
Control Parameters	PI controller (DC-link voltage controller)	$k_p^{v_{dc}}, k_i^{v_{dc}}$	4,30	5,50
	PI controller (Current Controller)	$k_p^{i_d}$, $k_i^{i_d}$, $k_p^{i_q}$, $k_i^{i_q}$	3,60,3,60	3,65,3,65
	PI controller (PLL)	k_p^{PLL}, k_i^{PLL}	5,100	2,120

2.5 Simulation and Experimental Analysis

To verify the effectiveness of the improved mathematical methodology and performance of the control strategy for the grid-tied PV system, simulation and experimental analysis have been carried out. The detailed system parameters of the grid-tied PV system used in the simulation and experiment are listed in Table 2.1.

2.5.1 Simulation Results

Detailed simulation studies are carried out on the MATLAB/Simulink platform, and the results obtained for various operating conditions are presented in this section. The improved mathematical methodology and the control strategy are executed under the software in the loop (SIL) environment using a real-time simulator OPAL-RT. The real-time simulation is performed with coordinated closed-loop control of MPPT controller, DC link voltage controller, and current controller by varying reactive power reference. Moreover, the values P_g and Q_g obtained in the MATLAB coding environment by the proposed mathematical methodology is validated by OP4510. The performance of the improved mathematical methodology and controller is analysed by considering two different case studies.

2.5.1.1 Grid-Tied PV System at Non MPP Condition Under Different Environmental Conditions.

In this case, the grid-tied PV system is simulated in OPAL-RT real-time simulator without considering the controller (open-loop control) and validated by the improved methodology for non MPP conditions. One of the real-time simulation results of the PV system for P_g and Q_g at $m_a = 0.8$ and $\delta = 0.1$, are shown in Fig. 2.9. It is illustrated in Fig. 2.9 that v_{pv}, P_g and Q_g are 826 V, 302 kW and 137 kVAR, respectively. Fig. 2.10 shows the curve of v_{PV} and δ for $m_a = 0.8$. It can be observed that v_{pv} decreases with the increase in δ. It is observed from Fig. 2.10 that for $\delta = 0.1$, $v_{PV} = 826$ V (shown by blue circle), which is same as the real-time simulation results of Fig. 2.11. The variation of P_g and Q_g with δ at $m_a = 0.8$ is shown in Fig. 2.11. It is noticed from Fig. 2.11 that MATLAB results of P_g and Q_g and real-time simulation values of P_g and Q_g (shown by black square and circle) for $\delta = 0.1$ are equal. It is noticed from Fig. 2.10 and Fig. 2.11 that the real-time simulation results are in close agreement with that of the results obtained by the MATLAB environment for the improved mathematical methodology. It has been observed that the reactive power decreases continuously with the increase in the values of δ, and P_G enhances with the increase in δ.

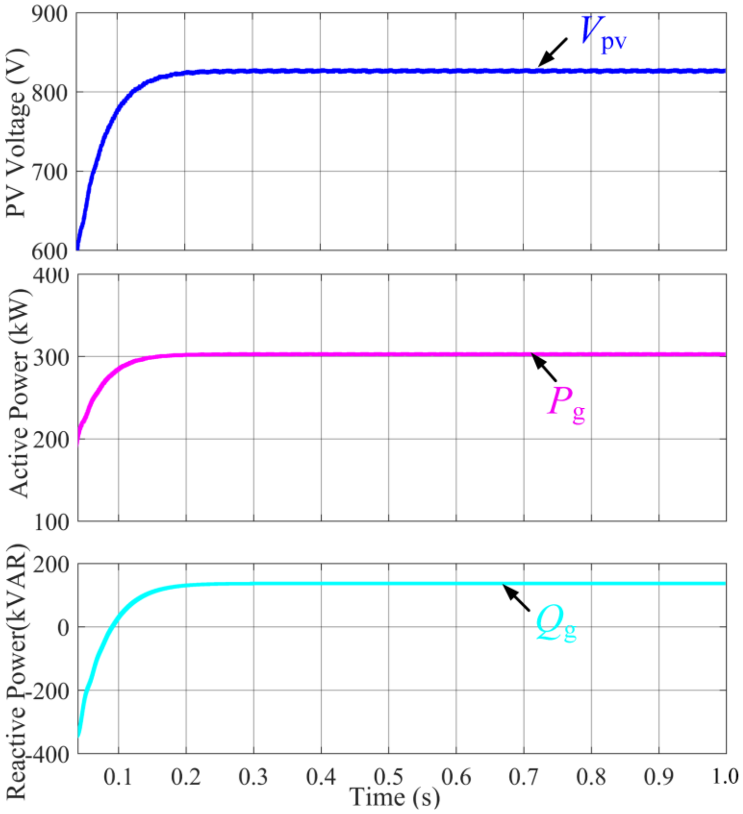

Fig. 2.9. Real-time simulated responses for: PV voltage(v_{pv}), Active power (P_g), Reactive power (Q_g) at $m_a = 0.8$ and $\delta = 0.1$.

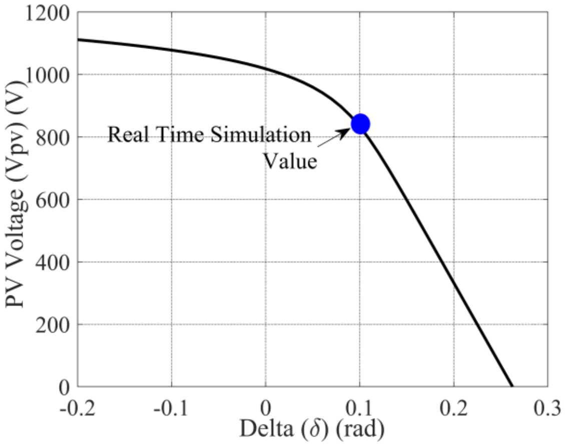

Fig. 2.10 PV voltage (DC) as a function of phase angle δ for $m_a = 0.8$.

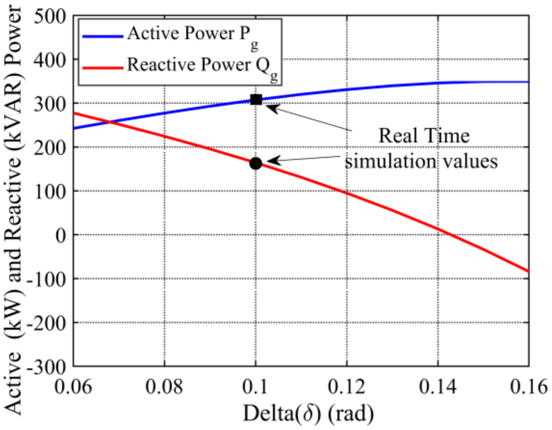

Fig. 2.11 Active power P_g and reactive power Q_g as a function of δ for m_a=0.8.

Fig. 2.12 illustrates the complete capability curve for different environmental conditions in the P_g- Q_g plane, where the modulation index is changed from 0.325 to 1. It can be noticed from Fig. 2.12 (a) that various capability curves have different values of m_a. Also, each capability curve having a constant m_a value has variation in δ. The complete capability curve is obtained from (2.31) - (2.34), discussed in section 2.4. The limits of reactive power output are -500 kVAR <Q< 500 kVAR, decided by limits of the inverter current. After constructing the P-Q capability curve of the inverter, it is essential to understand how these curves are useful to give information about the reactive power stability limit and reactive power reserve. The capability curve provides the range of reactive power for possible real power injected into the grid. It can be observed from Fig. 2.12 that the PV inverter injects positive active and reactive powers to the distribution grid in Region A. Moreover, the PV inverter consumes reactive power in region B. With the increase in reactive power (positive or negative), the real power injected to the grid decreases. It is noted from Fig. 2.12 that the grid injected active power is maximum, when the reactive power is zero. Moreover, it can be observed from Fig. 2.12 (a) and Fig. 2.12 (b) that the real power generation decreases with the decrease in irradiance and increase in temperature.

2.5.1.2 Grid-Tied PV System at MPP Condition Under Different Environmental Conditions

In this case study, the performance of the proposed methodology is verified by the real time simulation results of the grid-tied PV system using OPAL-RT. As the PV array is operated at MPP, the grid-tied PV system is simulated with closed loop control with MPPT controller, current controller, and DC link voltage controller. Fig. 2.13 demonstrate the characteristic between m_a and δ at the MPP condition. For maximum power condition, there will be only one δ for a particular value of m_a. These values of m_a, δ pairs of the curve are obtained from the improved mathematical methodology. For the validation, four m_a, δ pairs are chosen in Fig. 2.13 shown circles using four different colours. Fig. 2.14 shows the plot between δ, P_g and Q_g at maximum power condition with four calculated Q_g reference points shown by four circles corresponding to chosen m_a, δ pairs in Fig. 2.13.

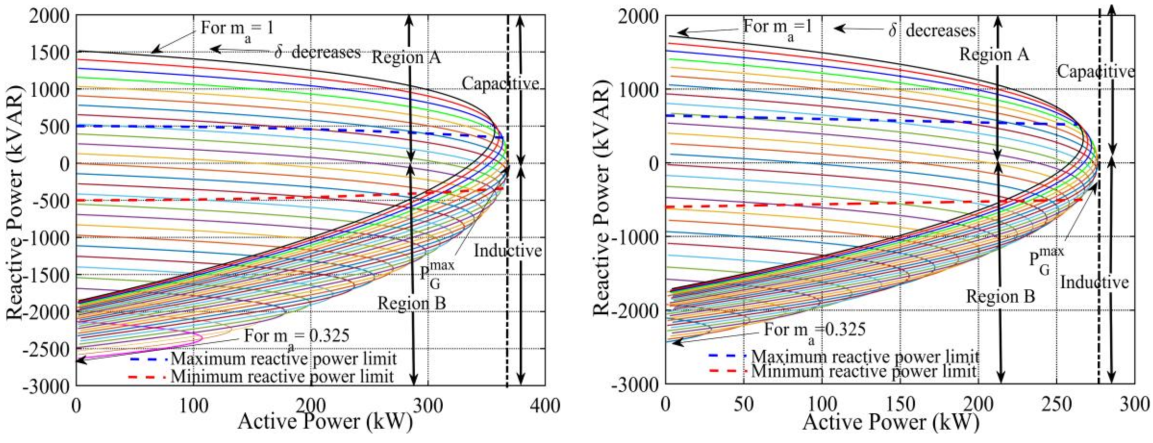

(a) **(b)**

Fig. 2.12. Total capability curve of the PV system for different environmental conditions (Non MPP condition) at **(a)** S= 1000 W/m^2, T= 25° C **(b)** S= 800 W/m^2, T= 40° C

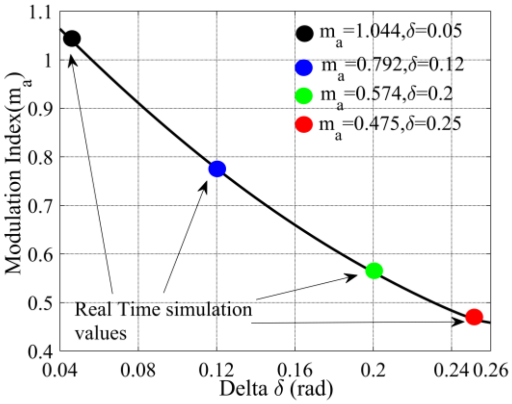

Fig. 2.13. Plot between m and δ at maximum power point condition (with MPP condition)

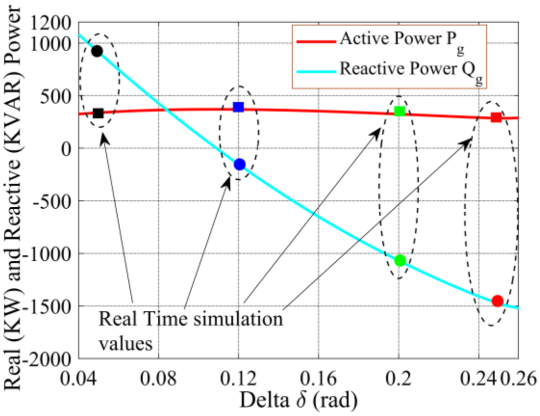

Fig. 2.14. Active power P_g and reactive power Q_g as a function of δ (with MPP condition)

Fig. 2.15 shows the real-time simulation results of the PV system at standard test condition (S = 1000 W/m^2 and T = 25° C) with MPP operation for four reference reactive powers (Q_{ref}) corresponding to four Q_g reference points (four circles) in Fig. 2.14. Initially, Q_{ref} is set at 912 kVAR, and the corresponding P_g and Q_g obtained are 331 kW and 912 kVAR, respectively. The PV voltage is settled at MPP voltage, v_{MPP} = 850 V. At t_1, Q_{ref} is changed to -153 kVAR and the corresponding P_g and Q_g become 369 kW and -153 KVAR, respectively. At the time instant t_2, Q_{ref} is changed to -1068 kVAR and the corresponding P_g and Q_g become 324 kW and -1068 kVAR, respectively. Finally, at the time instant t_3, the Q_{ref} is changed from -1068 kVAR to -1475 Kvar, which changes P_g from 324 kW to 288 kW and Q_g from -1068 kVAR to -1475 kVAR. It is observed from Fig. 2.15 that at time instant t_1, the reactive power decreases with the increase in real power injection to maintain the PV voltage at the MPP condition. Also, at time instant t_2 and t_3, with the decrease in real power injection, the reactive power for the PV inverter decreases for a fixed MPP voltage (V_{MPP}= 850 V). The value of four real powers obtained from OPAL-RT are shown using four squares in Fig. 2.14. This matches with the real powers obtained by the improved methodology as shown by the dotted lines. Thus, the value of P_g and Q_g obtained from MATLAB closely matches with those obtained from OPAL-RT, which validates the improved methodology.

The real-time simulated responses of modulation signals (m) for switching the IGBTs of the three-phase inverter of grid-tied PV are shown in Fig. 2.16. The values of m are obtained by changing the Q_{ref}. The modulation indices and phase shifts of these modulating signals are: m = 1.044, δ = 0.05; m = 1.044, δ = 0.05; m = 1.044, δ = 0.05 and m = 1.044, δ = 0.05. These four points correspond to the dots (squares for P_g and circles for Q_g) are shown in

Fig. 2.14. It is verified that the real-time simulation results and the results obtained by mathematical methodology from MATLAB results are similar. The zoomed view of Fig. 2.16 at two different reactive power references have been shown in Fig. 2.16(b) and Fig. 2.16(c), respectively. It can be noticed from Fig. 2.16(b) that at t_1, the values of m and δ are changed from $m = 1.044$ to 0.792 and $\delta = 0.05$ to 0.12. In the same way, it can be observed from Fig. 2.16(c) that at t_2, the values of m and δ are changed from 0.792 to 0.574 and 0.12 to 0.2, respectively.

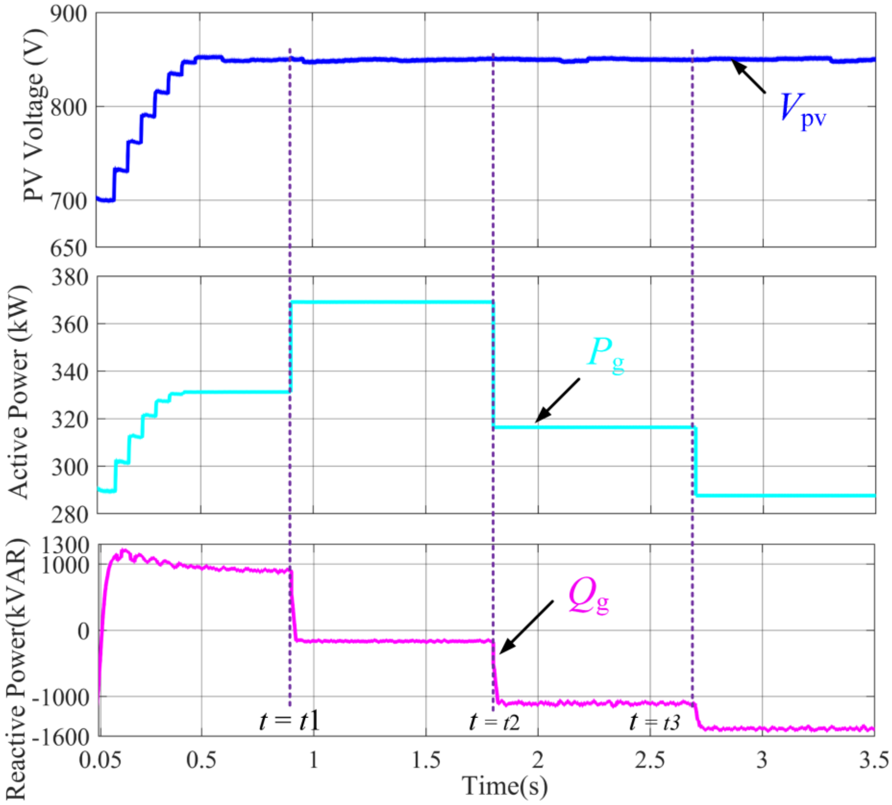

Fig. 2.15. Real-time simulated responses for: PV voltage(v_{pv}), Active power (P_g), Reactive power (Q_g).

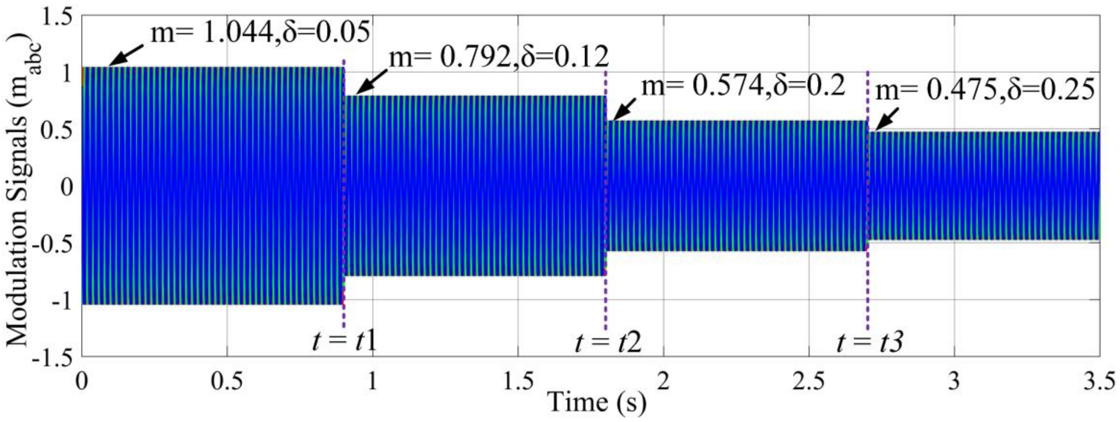

(a)

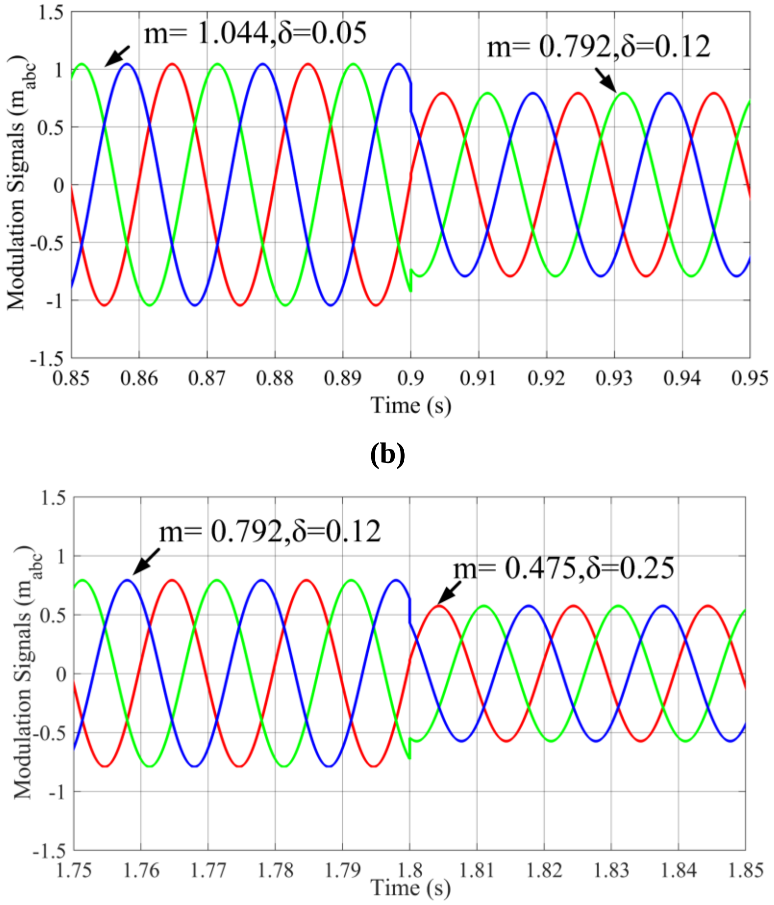

(b)

(c)

Fig. 2.16 Real-time Simulated responses of modulation waveforms (a) modulation variations, (b) Zoomed view of modulation variation from *m* = 1.044 to *m*=0.792, (c) Zoomed view of modulation variation from *m*= 0.792 to *m*=0.574

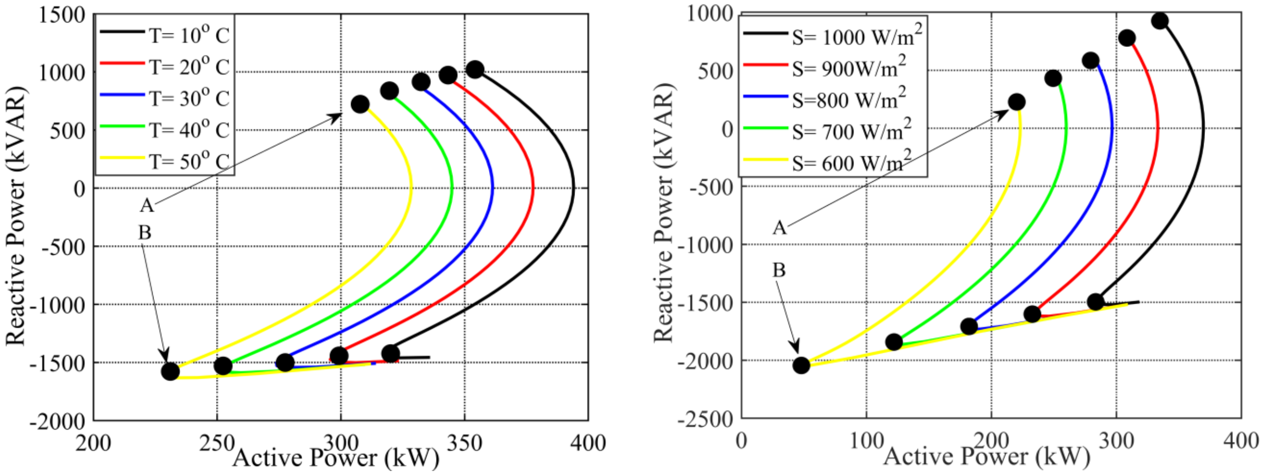

(a) **(b)**

Fig. 2.17 Reactive power limit for (a) Different temperature(s) level at constant irradiance (S= 1000 W/m^2), (b) Different irradiance(s) level at constant temperature (T= 25° C).

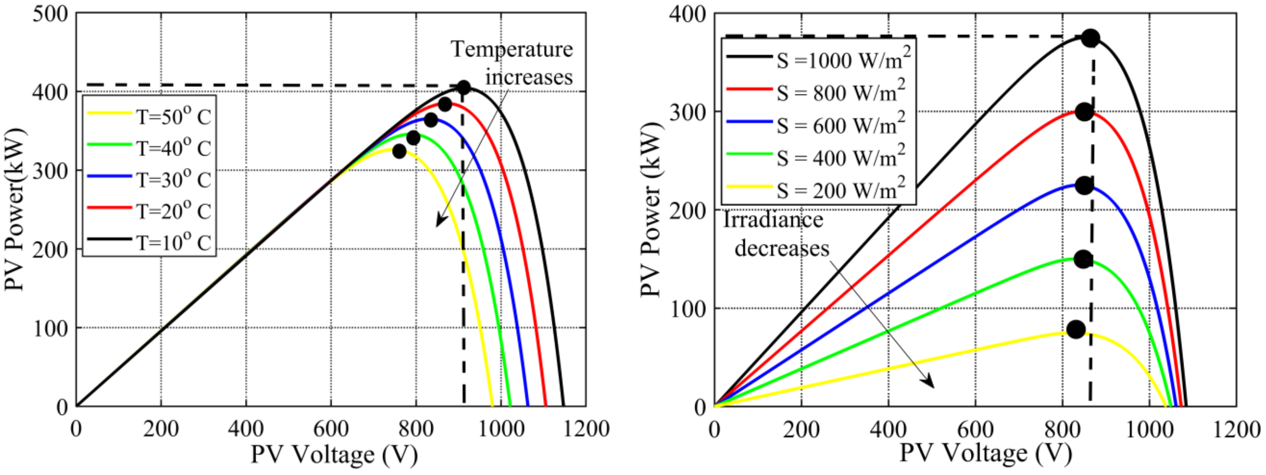

(a) **(b)**

Fig. 2.18. P vs V characteristics of PV module for (a) Different Temperature(s) level at constant irradiance (S= 1000 W/m^2), (b) Different irradiance(s) level at constant temperature (T= 25° C)

The full capability chart of the PV system with MPP conditions for different environmental conditions have been shown in Fig. 2.17. The P-Q capability curves serve as an effective tool to quickly give information about the system's operating point. It can be noticed from Fig. 2.19 (a)-(b) that the stable region for MPP operation in the capability curve lies between point A and point B. If any set of (P, Q) does not lie on the curve region between A and B, the whole PV system becomes unstable. The effect of temperature on full capability curve of the PV system is demonstrated in Fig. 2.17 (a). It is observed that the real and reactive power continuously decrease on increasing the temperature of PV module. The maximum power to be extracted by the PV system decreases as the temperature increases. In the same manner, the effect of insolation on full capability curve of the PV system can be seen in Fig. 2.17 (b). It can be observed that with the decrease in insolation, the active and reactive powers continuously decrease.

The behavior of voltage versus power for a different cell operating temperature at constant solar irradiance is also demonstrated in Fig. 2.18 (a). It is observed that with the increase in temperature, V_{MPP} and P_{MPP} decrease simultaneously. The change in cell temperature with constant irradiance has illustrated the significant effect on open-circuit voltage as well as the output power of the cell. Similarly, Fig. 2.18(b) represents the voltage versus power characteristics for different solar irradiance conditions at a constant cell temperature of the PV module. It has been observed that with a decrease in irradiance output power, V_{MPP} decreases simultaneously.

2.5.1.3 Dynamic Performance of the Grid-tied PV System under Different Environmental conditions

The dynamic performance of ASINC MPPT under variable atmospheric conditions is shown in Fig. 2.19. The scaling coefficient (n) of the ASINC MPPT method is considered as 0.07. Initially, the reference DC link voltage V_{dcref} = 700V for DC-link voltage controller, reactive power reference Q_{ref} is zero at temperature T = 25° C and irradiance S = 1000 W/m^2 are considered. Due to this, the PV array power P_{pv} and the grid injected reactive power Q_{g} are 330 kW and 0 KVAR, respectively, as shown in Fig. 2.19.

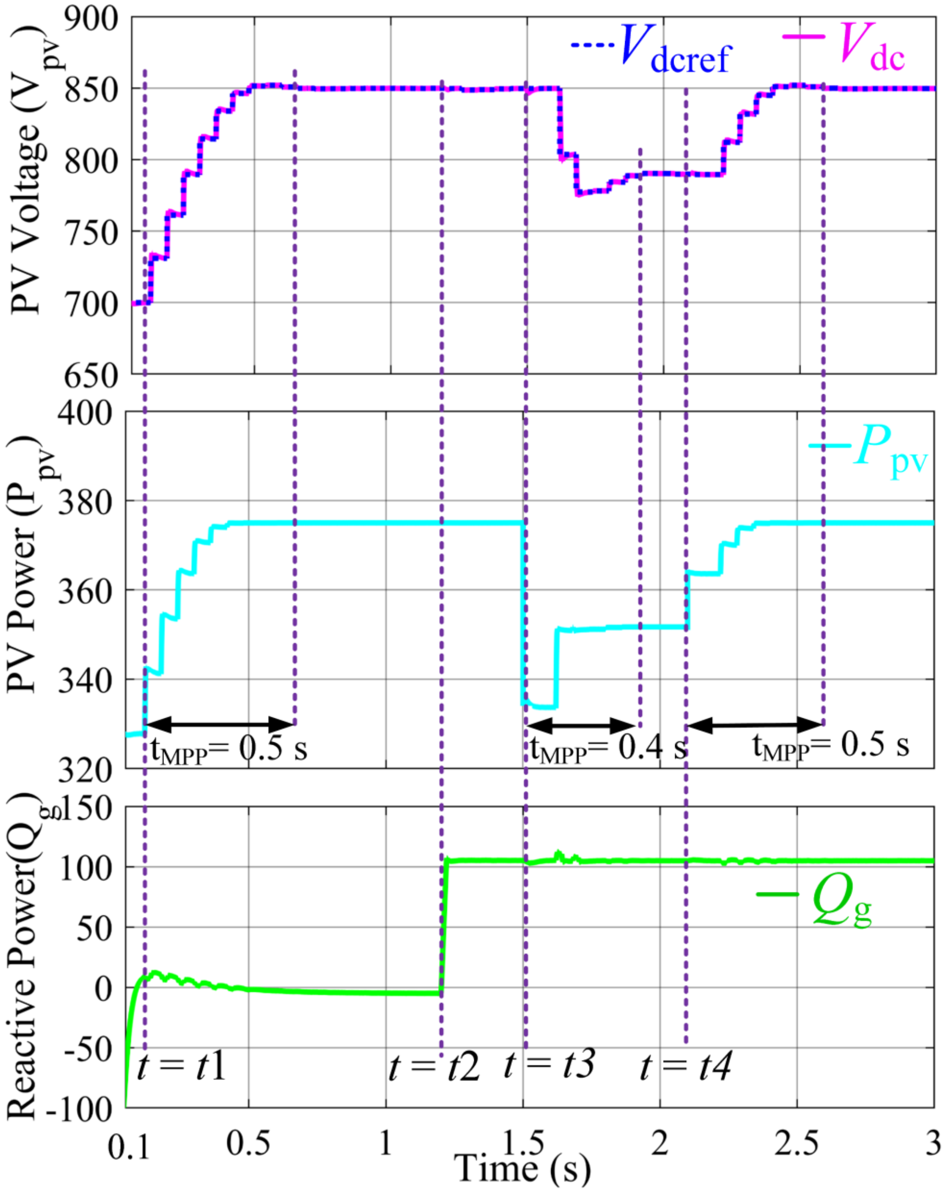

Fig. 2.19. Dynamic performance of ASINC MPPT under variable atmospheric condition: DC voltage (V_{dc}), reference DC voltage (V_{dcref}), PV array Power (P_{PV}) and grid injected reactive Power (Q_{g}).

At $t = t_1$, the ASINC MPPT algorithm is applied and regulates V_{dcef} to MPP voltage $V_{MPP} = 850$ V. As V_{dcref} increases, P_{pv} increases and becomes equal to the maximum value 375 kW at V_{MPP}. However, the injected reactive power to the gird Q_g is 0 KVAR. Thus, shows decoupling of real and reactive power controllers. The tracking time to reach the MPP voltage is $t_{MPP} = 0.5$ s. Moreover, it is noticed that the oscillations are negligible near MPP voltage ($V_{MPP} = 850$ V). At $t = t_2$, the reactive reference power Q_{ref} is changed to 200 KVAR from 0 KVAR and Q_g is changed from 0 to 200 kVAR. The disturbances in V_{dc} and P_{PV} are almost insignificant due to the decoupling between the active and reactive power controllers in the system. At $t = t_3$, the atmospheric condition is changed as S changes from 1000 W/m^2 to 400 W/m^2 and T changes from 25° C to 50° C. The new V_{MPP} (790 V) is tracked by the MPPT controller and the tracking time $t_{MPP} = 0.4$ s. Hence, it can be stated that the modified MPPT INC method has good dynamic performance. It is clear that very small (insignificant) disturbance has occurred in Q_g, when P_{pv} is decreased from 375 kW to 352 kW because of the decoupling effect between active and reactive power controllers. At $t = t_4$, the atmospheric condition is again changed due to the variation in S from 400 W/m^2 to 1000 W/m^2 and T from 50° C to 25° C. It is observed that V_{DCref} settles at new MPP voltage, $V_{MPP} = 850$ V with $t_{MPP} = 0.5$ s. Similarly, P_{pv} changes to 352 kW from 375 kW.

2.5.2 Experimental Verifications

To verify the simulation results, the experimental tests are carried out on a laboratory prototype of 3.75 kW as shown in Fig. 2.20. The grid voltage is generated by a three-phase grid simulator ITEC. The solar power generation is emulated using a programmable solar PV simulator Chroma 62100H-600S. The prototype consists of a SEMIKRON SM150GB 12T4 power module, including six insulated gate bipolar transistors (IGBT) and gate drivers with a protection circuit. The proposed control strategy is executed under the hardware in the loop (HIL) environment of the digital simulator OPAL-RT OP4510. The experimental waveforms of v_{pv}, P_g and Q_g at $m = 0.85$ and $\delta = 0.12$ are shown in Fig. 2.21. It is observed that the v_{pv} , P_g and Q_g are 410 V, 3.02 kW and 1.37 kVAR, respectively. The dynamic experimental responses of grid-tied PV system with coordinated control of MPPT controller, current controller and DC link voltage controller under MPP condition is shown in Fig. 2.24. Four sets of Q_{gref} at MPP have been evaluated using the improved methodology. Consequently, with these sets of Q_{gref}, the corresponding P_g at MPP condition are experimentally verified as depicted in Fig. 2.22. Initially, Q_{ref} is set to 9.12 kVAR, and the corresponding P_g and Q_g obtained are 3.31 kW and 9.12 kVAR. The PV voltage is settled at MPP voltage, $v_{\mathrm{MPP}} = 430$ V. At t_1, Q_{ref} is changed to -1.53 kVAR and the corresponding P_g and Q_g become 3.69 kW and -1.53 KVAR. At the time instant t_2, Q_{ref} is changed to -10.68 kVAR and the corresponding P_g and Q_g become 3.24 kW and -10.68 kVAR. Finally, at the time instant t_3, the Q_{ref} is changed from -10.68 kVAR to -14.75 kVAR, which changes the P_g from 3.24 kW to 2.88 kW and Q_g from -10.68 kVAR to -14.75 kVAR. It is noticed from Fig. 2.22 at t_1 that the reactive power decreases with the increase of real power injection to maintain the PV voltage at MPP condition. In addition, at t_2 and t_3, with the decrease in real power injection, the reactive power of the PV inverter decreases for a constant MPP voltage $V_{\mathrm{MPP}} = 430$ V. The experimental waveforms of modulation signals m for the VSI of grid-tied PV system are presented in Fig. 2.23. The values of m are obtained by changing Q_{ref} at the MPP condition. The modulation indices and phase shifts of these modulating signals obtained are: $m = 1.044$, $\delta = 0.05$; $m = 1.044$, $\delta = 0.05$; $m = 1.044$, $\delta = 0.05$ and $m = 1.044$, $\delta = 0.05$. These values are obtained from the four sets of values of Q_{ref} at MPP condition as shown in Fig. 2.22. The zoomed views of Fig. 2.22 at two different values of Q_{ref} have been shown in Fig. 2.23(b) and Fig. 2.23 (c).

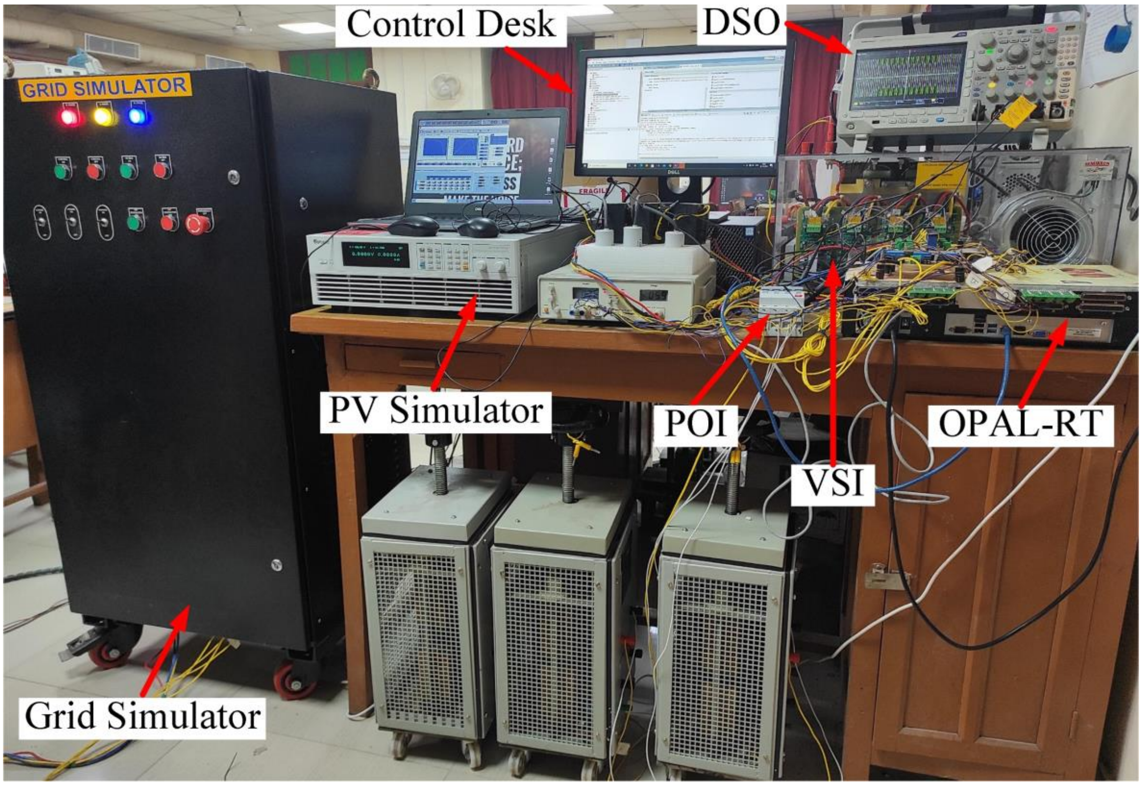

Fig. 2.20. Photograph of the experimental setup for the grid-tied PV system.

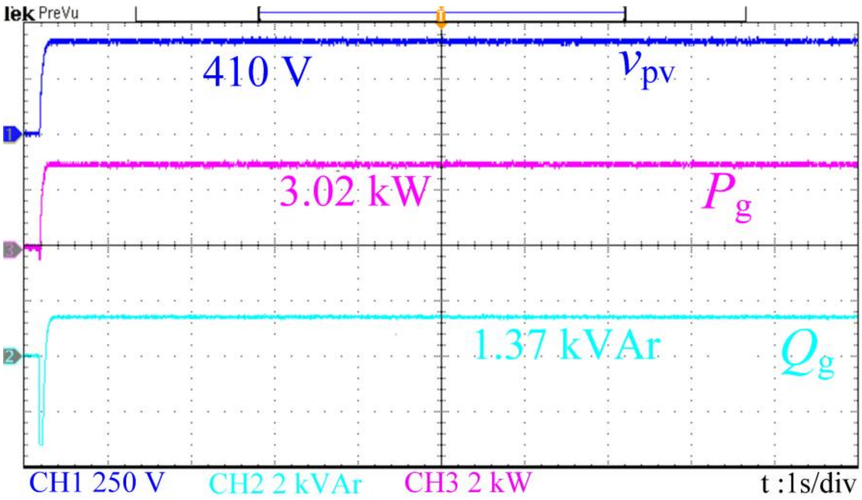

Fig. 2.21. Experimental waveforms for: PV voltage (v_{pv}), active power (P_g), reactive power (Q_g) at $m = 0.85$ and $\delta = 0.12$.

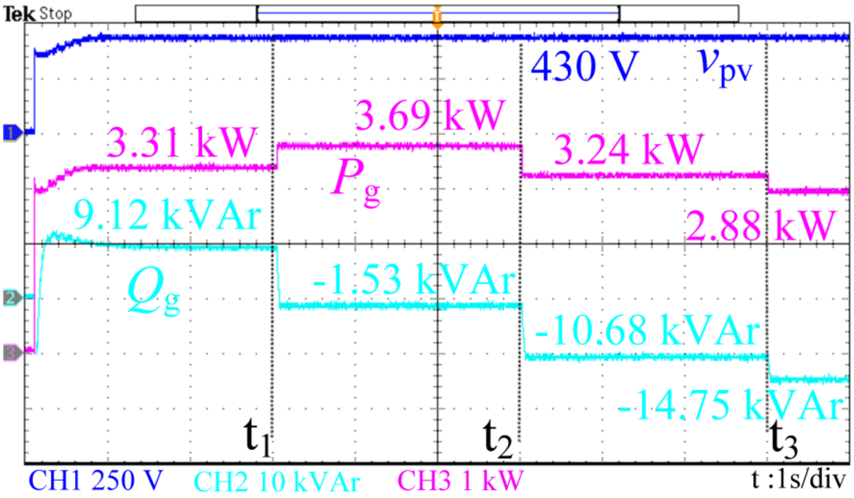

Fig. 2.22. Dynamic experimental responses of grid-tied PV system at MPP for: PV voltage (v_{pv}), active power (P_g), reactive power (Q_g).

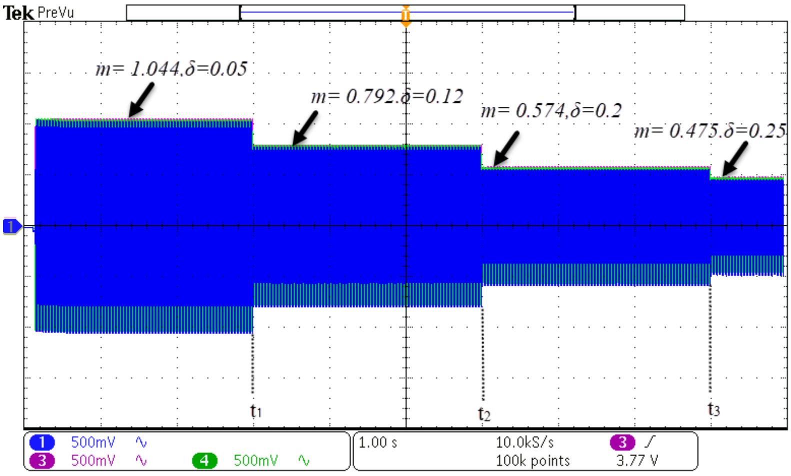

(a)

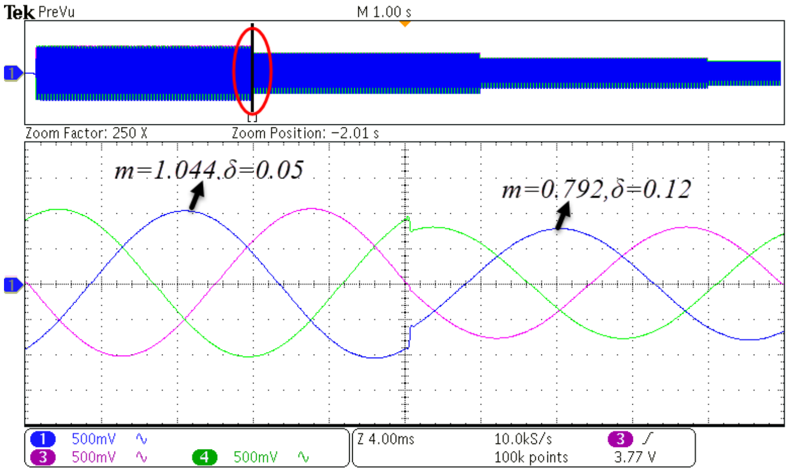

(b)

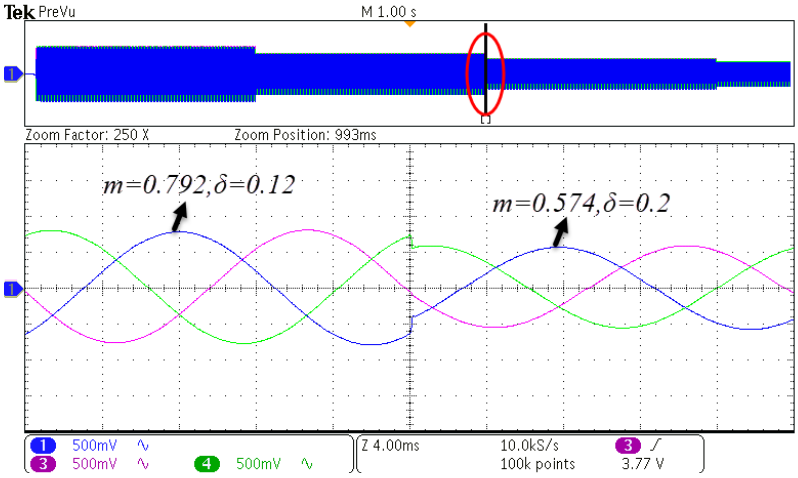

(c)

Fig. 2.23. Experimental waveforms of modulation waveforms (a) modulation variations, (b) zoomed view of modulation variation from m= 1.044 to m=0.792, (c) zoomed view of modulation variation from m= 0.792 to m=0.574.

2.6 Conclusion

In this chapter, an improved mathematical methodology is proposed to obtain the *P-Q* capability curve under the maximum power point condition for a single-stage grid-tied PV system operated with a coordinated control strategy. The overall control strategy regulates the active and reactive powers injection into the distribution grid. The *P-Q* capability curve provides reactive power limits under MPP conditions and is used to improve the management of reactive power compensation and active power generation of the grid-tied PV system. The capability curve of the PV inverter at MPP condition considering the variation of solar irradiance and temperature has been analyzed. The performance analysis of the improved methodology and the coordinated control strategy are carried out using real-time simulations. They are finally verified through experimentation using the OPAL-RT digital simulator. The effectiveness of the proposed methodology is verified by changing reference reactive power Q_{ref} to the grid. Due to the change in the value of the reactive power references, the grid injected active power P_{g}, modulation index m and the phase angle δ are changed. The changed values obtained from experimental results match the corresponding values acquired from the proposed methodology.

The improved methodology provides the basics for deciding the current reference for controllers according to the power limits and manages the current injection into the grid from PV system. The current controller, DC-link voltage controller and MPPT controller are coordinately operated and maintain the power quality when the grid voltage is balanced and is free from harmonics. However, grid voltage consists of common issues like harmonics distortions, unbalanced conditions, voltage sag and swell conditions. In such cases, significant amount of harmonics in the grid injected current and large power oscillations are present with the coordinated control strategy. Consequently, the distorted grid voltages seriously affect the grid-tied inverters, resulting in increased current harmonics. The current harmonics increase the losses, heating on the equipment, reducing the equipment’s life span, and affecting the control and protection circuits of the grid-tied PV system. In order to improve the injected grid current quality, modifications in the basic control strategy are an immediate requirement. Therefore, an advanced control strategy to regulate the grid current of the grid-tied PV system under unbalanced grid voltage conditions is presented in chapter 3.